

Effect of Periodicity in the Resonant Scattering of Light by Finite Sparse Configurations of Many Silver Nanowires

Denys M. Natarov · Ronan Sauleau · Marian Marciniak · Alexander I. Nosich

Received: 5 August 2013 / Accepted: 7 November 2013 / Published online: 11 December 2013
© Springer Science+Business Media New York 2013

Abstract We consider the two-dimensional (2-D) scattering of the H- and E-polarized plane waves by several discrete configurations made of $M \gg 1$ periodically arranged circular cylindrical silver wires. To find the scattered field, we use the field Fourier expansions in local coordinates and addition theorems for cylindrical functions. Resulting $M \times M$ block-type matrix equation is cast to the Fredholm second-kind form that guarantees convergence of numerical solution when each block is truncated to finite dimensions and truncation order is taken larger. The scattering and absorption cross-sections and the near-field patterns are computed. The interplay of plasmon and grating-type resonances is studied for finite in-line and stacked arrays, corners, and crosses made of nano-size silver wires in the visible range of wavelengths, with the refractive index of silver taken from the experimental data.

Keywords Wave scattering · Absorption · Silver wire · Finite grating · Plasmon resonance · Grating resonance

Introduction

Periodically structured metallic and dielectric scatterers including gratings, arrays or chains of particles, and holes in the screens (in

3-D) or wires and slots (in 2-D) are attracting large attention of researchers in today's nanophotonics—for instance, see [1–25]. This is caused by the effects of extraordinarily intensive reflection, transmission, emission, and near-field enhancement that have been found in the scattering of light by periodic scatterers. A certain controversy still exists around the explanation of these phenomena. If the particles or wires are metallic and the distance between the neighboring elements is small in comparison to the period (dense gratings), so that the scatterer can be viewed as a perforated metal slab, the mentioned effects are frequently attributed to the excitation of the delocalized surface-plasmon waves on both sides of the periodically deformed slab. This explanation is not free of ambiguity [26] and clearly does not work out well if the elements of the grating are well separated one from another (sparse gratings). In that case, it is more natural to talk about the excitation of the localized surface plasmon oscillations on each metal element of the grating. However, this mechanism cannot explain all associated effects, especially if a grating of subwavelength metal scatterers is located in a homogeneous medium, i.e., is not supported by a dielectric substrate; it fails completely if a grating is made of purely dielectric elements.

Recently, a growing understanding has emerged that the mentioned optical effects can be attributed to the so-called grating resonances (a.k.a. geometrical, collective, lattice, trapped-mode, and Bragg resonances [1–25]) explained by the existence of specific poles of the field as a function of wavelength [16–19, 24, 25]. If the size of elementary scatterer is a fraction of the period, their wavelengths are just above (however do not coincide with) the Rayleigh wavelengths $\lambda_{RA}^{\pm m} = (p/m)(1 \pm \cos \varphi_0)$, $m = 1, 2, \dots$, where p is the period and φ_0 is the angle of a plane-wave incidence counted from the grating. The values of $\lambda_{RA}^{\pm m}$ appear in the theory of wave scattering by infinite gratings and are the real-valued branch points for the field function. They are known as those in which one of the higher diffraction orders (Floquet harmonics) is “passing over the horizon”, i.e., is approaching the onset of radiation [27]. For the normal incidence of a plane wave, these

D. M. Natarov (✉) · A. I. Nosich
Institute of Radio-Physics and Electronics, National Academy
of Sciences of Ukraine, Kharkiv 61085, Ukraine
e-mail: den.natarov@gmail.com

R. Sauleau
Institute of Electronics and Telecommunications,
Université de Rennes 1, Rennes, France

M. Marciniak
National Institute of Telecommunications, Szachowa 1,
Warsaw 04-894, Poland

M. Marciniak
Kielce University of Technology, Al. Tysiaclecia Panstwa
Polskiego 7, Kielce 25-314, Poland

values are integer divisions of the grating period, p/m , $m=1, 2, \dots$. Unlike the branch points at $\lambda_{RA}^{\pm m}$, the grating mode poles have complex wavelengths corresponding to the radiation losses. They have been found explicitly, in the form of asymptotic series, for the infinite grating of circular wires in [17] and of thin flat strips in [24]. In the plane-wave scattering by infinite gratings, these poles lead to almost total reflection of the incident field by a sparse grating of subwavelength elements in a narrow band [1–25]. Important is that the grating mode resonances of enhanced reflection have been found on the gratings made of both metallic and dielectric elements and in the latter case in the both of two alternative polarizations [1, 3, 7, 16–19, 22].

As mentioned above, there exist the scattering resonances of another type, better known by now, which are caused by localized surface plasmon modes (plasmons, for brevity)—they are observed on stand-alone subwavelength particles and wires provided that they are made of noble metals (for instance, silver and gold) in the mid-infrared and optical bands [28]. In the case of wires or strips that are infinite along one dimension in 3-D space, plasmon resonances exist only in the H-polarization, i.e., when the electric field is normal to the wires. These resonances are electrostatic in nature [29], therefore, in the leading terms, the plasmon resonance wavelengths depend on the noble metal object shape but not on its dimensions. Excitation of plasmons results in powerful enhancement of scattered and absorbed light that is used in the design of optical antennas, biochemical sensors, broadband ultra-thin absorbers, and other advanced applications.

Quite naturally, if a periodic array is made of many noble metal elements of subwavelength size, both type of resonances (i.e., associated poles of the field function) exist together. Apparently because of this, the grating resonances had been frequently misinterpreted either as an effect of specific plasmons [4–6, 10–12, 14, 15, 21] or of Rayleigh anomalies [14, 23]. Still another important question is how large a finite grating should be to develop observable grating resonances in the scattering and absorption. The scattering properties of pairs (a.k.a. dimers), short arrays, and clusters of metal nanowires are well documented (see [30–32]) and reveal only the hybridization of conventional plasmon resonances. This means the formation of the so-called supermodes split into

different classes of symmetry and having the wavelengths, which are red-shifted and blue-shifted with respect to the similar mode of a stand-alone wire. Therefore, it is clear that, to be observable, the grating resonances need large number of elementary scatterers.

In the paper [17], we have presented an improved algorithm able to compute finite-size collections of dielectric or metal wires of circular cross-section and applied it to the study of the H-polarized wave scattering by finite one-periodic gratings of silver nanowires in the visible range. We have found an interesting interplay of the low-quality plasmon resonances on each nanowire and the grating resonances, whose Q-factors become quite large if the number of wires in the grating goes to dozens and hundreds.

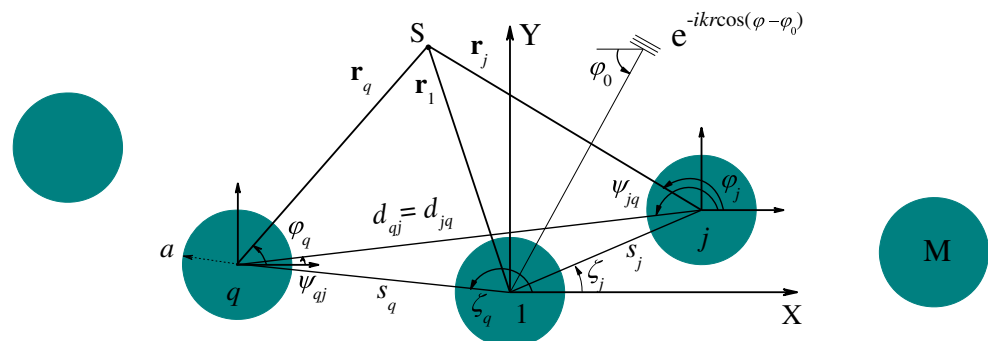
The goal of our paper is to study several more complicated periodically structured configurations of parallel silver wires of circular cross-section. This includes the scatterers that contain not a single but two gratings with the same or different periods, stacked or in-line, and also finite periodic corners and crosses. Besides, we consider briefly the E-polarized plane wave excitation of silver-wire gratings in the free-space environment where plasmon modes do not exist and the grating modes have too small Q-factors to be visible in the scattering and absorption characteristics.

Generic Scattering Problem

Formulation and Basic Equations

Consider a finite collection of M parallel wires illuminated by a plane wave as shown in Fig. 1. The wires are assumed to be identical infinite circular cylinders, each having radius a and complex relative dielectric permittivity $\varepsilon = \nu^2$, where ν is refractive index. It is convenient to introduce M local Cartesian (x_q, y_q) and polar coordinates (r_q, φ_q) , $q=1, \dots, M$ with the origins in the centers of each of M wires, and also the global coordinates with the origin, say, in the center of the wire number 1. As known, for a 2-D problem, two alternative field polarizations are essential: one deals with the light that is polarized across the wires (H-polarization) and the other with

Fig. 1 Cross-sectional geometry of the M -wire scattering problem and notations used



the light polarized along the wires (E-polarization). In the H-case, one has to find a scalar function $H_z(\vec{r})$ that is the scattered magnetic field z -component. It must satisfy the 2-D Helmholtz equation with wavenumbers $k\nu$ and k inside and outside the cylinders, the tangential field components continuity conditions on the wire contours, the radiation condition at infinity, and the condition of the local power finiteness. These conditions guarantee the solution uniqueness.

The full-wave numerical solution can be obtained, similarly to [33–39], by expanding the field function in terms of the Fourier series in azimuth exponents in the local polar coordinates associated with each wire (Fig. 1).

$$U^{int(q)}(r, \varphi) = \sum_{n=-\infty}^{\infty} y_n^{(q)} J_n(k\nu r_q) e^{in\varphi_q}, r_q < a, q = 1, \dots, M \quad (1)$$

$$U^{ext}(r, \varphi) = U^0 + \sum_{q=1}^M \sum_{n=-\infty}^{\infty} z_n^{(q)} H_n^{(1)}(kr_q) e^{in\varphi_q}, r_q > a \quad (2)$$

where $U^0 = \exp[-ikr \cos(\varphi - \varphi_0)]$ is the incident-wave field function.

On using the addition theorems for cylindrical functions,

$$H_n^{(1)}(kr_q) e^{in\varphi_q} = \sum_{m=-\infty}^{+\infty} J_m(kr_j) H_{m-n}^{(1)}(kd_{jq}) e^{i(n-m)\psi_{jq}} e^{im\varphi_j}, r_q > r_j, \quad (3)$$

applying the boundary conditions on the surface of each of M wires,

$$U(r_q = a + 0) = U(r_q = a - 0), \quad \partial U / \partial r_q |_{r_q=a+0} = \varepsilon^{-1} \partial U / \partial r_q |_{r_q=a-0} \quad (4)$$

and introducing the constants $\beta^{E,H} = \nu^{\pm 1}$, one obtains an $M \times M$ block-type matrix equation where each block is infinite,

$$Z + PX = Q, \quad (5)$$

$$Z = \left\{ Z^{(q)} \right\}_{q=1}^M, \quad Z^{(q)} = \left\{ z_m^{(q)} \right\}_{m=-\infty}^{+\infty} \quad (6)$$

$$P = \left\{ P^{(q,j)} \right\}_{q,j=1}^M, \quad P^{(q,j)} = \left\{ P_{m,n}^{(q,j)} \right\}_{m,n=-\infty}^{+\infty}, \quad Q = \left\{ Q^{(q)} \right\}_{q=1}^M, \quad Q^{(q)} = \left\{ \tilde{B}_m^{(q)} \right\}_{m=-\infty}^{+\infty}, \quad (7)$$

$$P_{m,n}^{(q,j)} = \frac{H_{n-m}^{(1)}(kd_{jq}) V_m(ka, \nu)}{F_m(ka, \nu)} e^{i(m-n)\psi_{jq}}, \quad \tilde{B}_m^{(q)} = \frac{(-i)^m V_m(ka, \nu)}{F_m(ka, \nu)} e^{-iks_q \cos(\zeta_q - \varphi_0) - im\varphi_0} \quad (8)$$

$$F_m^{E,H} = \beta^{E,H} H_m^{(1)}(ka) J'_m(\nu ka) - H_m^{(1)'}(ka) J_m(\nu ka) \quad (9)$$

$$V_m^{E,H} = \beta^{E,H} J_m(ka) J'_m(\nu ka) - J'_m(ka) J_m(\nu ka) \quad (10)$$

The matrix Eq. (5) or similar ones can be found in the great majority of the previous papers (see, for instance, [33–39]). They have been used to generate many numerical results that seem reasonable, although some of the authors complained to what they called “accumulation of round-off errors” when the block truncation number N was taken larger. A close inspection shows that (5) cannot guarantee the convergence of numerical solutions. Here, we understand the convergence in mathematical sense, as a possibility of minimizing the error of computations by solving progressively larger matrices. Frequently, convergence is mixed up with accuracy. Many divergent numerical schemes are able to provide a few first digits correctly; however, fail when a better accuracy is required. Indeed, the matrix elements in (5) decay along the columns (i.e., with index m), however, exponentially grow along the lines (i.e., with index n).

Therefore, strictly speaking, one cannot replace the matrix (5) with a truncated counterpart. This behavior of solutions of (5) has been studied in [39] where it is demonstrated that the best achievable accuracy at “too large” values of N is somewhere around 10^{-2} —see section 3.4 of [39].

The reason of this poor performance is easily understood: the boundary conditions at the q th wire contour bring together two coefficients in each azimuth order n : $y_n^{(q)} J_n(k\nu a)$ and $z_n^{(q)} H_n^{(1)}(ka)$. To satisfy this condition for large n , the coefficients $y_n^{(q)}$ must balance the exponential decay of the Bessel functions for $n \gg k\nu a$ while the coefficients $z_n^{(q)}$ must balance the exponential growth of the Hankel functions. When these oppositely behaving coefficients are collected together, the common matrix equation happens to be misbalanced and cannot be truncated to provide convergence.

We have found, however, that this defect of earlier publications can be fixed by re-scaling the unknown coefficients. Indeed, we introduce new unknowns $x_n^{(q)}$ as follows:

$$z_n^{(q)} = x_n^{(q)} J_n(ka) \quad (11)$$

The obtained, in such a way, matrix equation

$$X + AX = B, \tag{12}$$

$$X = \left\{ X^{(q)} \right\}_{q=1}^M, \quad X^{(q)} = \left\{ x_m^{(q)} \right\}_{m=-\infty}^{+\infty} \tag{13}$$

$$A = \left\{ A^{(q,j)} \right\}_{q,j=1}^M, \quad A^{(q,j)} = \left\{ A_{m,n}^{(q,j)} \right\}_{m,n=-\infty}^{+\infty}, \quad B = \left\{ B^{(q)} \right\}_{q=1}^M, \quad B^{(q)} = \left\{ B_m^{(q)} \right\}_{m=-\infty}^{+\infty}, \tag{14}$$

$$A_{m,n}^{(q,j)} = \frac{H_{n-m}^{(1)}(kd_{jq}) V_m(ka, \nu) J_n(ka)}{F_m(ka, \nu) J_m(ka)} e^{i(m-n)\psi_{jq}}, \quad B_m^{(q)} = \frac{(-i)^m V_m(ka, \nu)}{F_m(ka, \nu) J_m(ka)} e^{-iks_q \cos(\zeta_q - \varphi_0) - im\varphi_0} \tag{15}$$

is a block-type Fredholm second kind equation that follows from the properties

$$\sum_{n,m=-\infty}^{+\infty} |A_{mn}^{(q,j)}|^2 < \infty, \quad \sum_{m=-\infty}^{+\infty} |B_m^{(q)}|^2 < \infty, \quad (q, j = 1, \dots, M) \tag{16}$$

which hold true provided that all $d_{jq} > 2a$, i.e., if the wires do not touch each other. This can be proved analytically after replacing the cylindrical functions with the first terms of the corresponding series in powers of the arguments.

After rescaling, the Fredholm theorems of the operator analysis guarantee that the solution of Eq. (12) with each block truncated to finite order N converges to exact solution if $N \rightarrow \infty$. This is the property which does not hold for the solutions of truncated Eq. (5).

The results presented below were computed with $N=4-6$; this provided three correct digits in the far-field characteristics of the sparse gratings of silver wires with radii $a \leq 75$ nm and periods $p \geq 200$ nm. We have considered three sparse ($p - 2a > a$) configurations of finite number of subwavelength silver nanowires as follows: linear gratings (discrete line), discrete right-angle corners, and discrete crosses—see Fig. 2. Dense configurations are also interesting objects; however, they deserve a separate study; they need larger values of N to achieve the same accuracy.

The scattered field is represented by the second term in (2). In the far zone, large-argument asymptotics of the Hankel functions lead to the following outgoing cylindrical wave representation, with $\Phi(\varphi)$ being the scattering pattern as follows:

$$U^{sc}(r, \varphi) \sim \left(\frac{2}{i\pi kr} \right)^{1/2} \Phi(\varphi), \quad \Phi(\varphi) = \sum_{n=-\infty}^{+\infty} (-i)^n J_n(u) \left[\sum_{q=1}^M x_n^{(q)} e^{-i2\pi\kappa s_q \cos(\zeta_q - \varphi)} \right] e^{in\varphi} \tag{17}$$

The scattering properties of finite-size objects are conventionally characterized with the aid of the total scattering cross-section (TSCS) and absorption cross-section (ACS),

$$\sigma_{sc} = \frac{2}{\pi k} \int_0^{2\pi} |\Phi(\varphi)|^2 d\varphi \tag{18}$$

$$\sigma_{abs} = \frac{2\pi a}{|\nu|^2} \sum_{q=1}^M \sum_{n=-\infty}^{+\infty} |y_n^{(q)}|^2 \text{Im} \left[\nu J_n(ka\nu) J_n'(ka\nu^*) \right] \tag{19}$$

It should be also noted that the sum of the latter two values is called the extinction cross-section. The Green's formula,

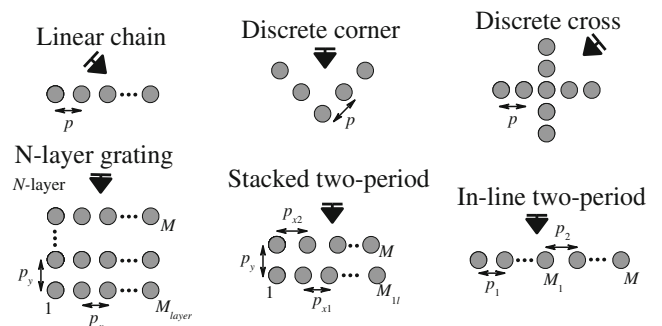


Fig. 2 Cross-sectional geometries of the discrete-wire configurations considered in the paper

applied to the total-field function and its complex-conjugate counterpart in a finite domain whose outer boundary is stretched to infinity, leads to the so-called Complex Poynting Theorem [40]. If the incident field is a plane wave, then some of the associated integrals can be taken analytically and the extraction of the real part of the final expression yields the Optical Theorem. According to it, extinction is directly responsible for the scattered-field amplitude in the *forward direction*, i.e., at the angle of $\varphi_0 + \pi$, in our notations as follows:

$$\sigma_{sc} + \sigma_{ab} = -(4/k)\text{Re} \Phi(\varphi_0 + \pi) \tag{20}$$

Interestingly enough, recalling that the forward direction is the direction of the *shadow beam* of the far-field scattering pattern, $\Phi(\varphi)$, one can conclude that both components of extinction are equally responsible for the shadow of the object illuminated by a plane wave. Expression (20), together with (18) and (19) can be used for a partial validation of the numerical results. In the computations presented below, the identity (20) has been satisfied with accuracy close to machine precision. Thanks to this property, one can compute ACS not by using relatively slow-convergent series (19) but as a difference between the right-hand part of (20) and σ_{sc} .

The complex-valued dielectric function of silver in the visible range was taken from paper [41] and supplemented with Akima spline code to provide the values between the experimental points.

Results and Discussion

Two-Layer and Three-Layer Gratings

We have considered the optical resonances on a single row of periodically placed circular silver nanowires in [17, 18]. This study has shown that the optimal radius of the wires is between 30 and 70 nm, and the minimum number of wires necessary to produce well-observable grating resonances lies between 100 and 20, respectively. Keeping this in mind, we have computed the scattering of an H-polarized plane wave by finite gratings

consisting of two and three parallel rows of identical wires, in the wavelength range between 300 and 500 nm—see Figs. 3 and 4.

If the wire positions along the rows of two-layer grating (i.e., the x -coordinates) coincide for the lower and upper row, then such a grating can be viewed as consisting of $M_{\text{layer}} = M/2$ dimers (pairs of wires with the distance along the y -axis between their centers, or the gap, p_y) located with period p_x along the x -axis. Similarly, a three-layer grating has $M_{\text{layer}} = M/3$ trimers, i.e., three-wire sub-arrays aligned in parallel to the y -axis. In Fig. 3a, we present the plots of TSCS of such configurations, normalized by the total number of wires M , as a function of the wavelength, illuminated in broadside manner ($\varphi_0 = \pi/2$). All plots show broad resonance peaks near to $\lambda = 340$ nm—this is the plasmon resonance on each on the silver nanowires.

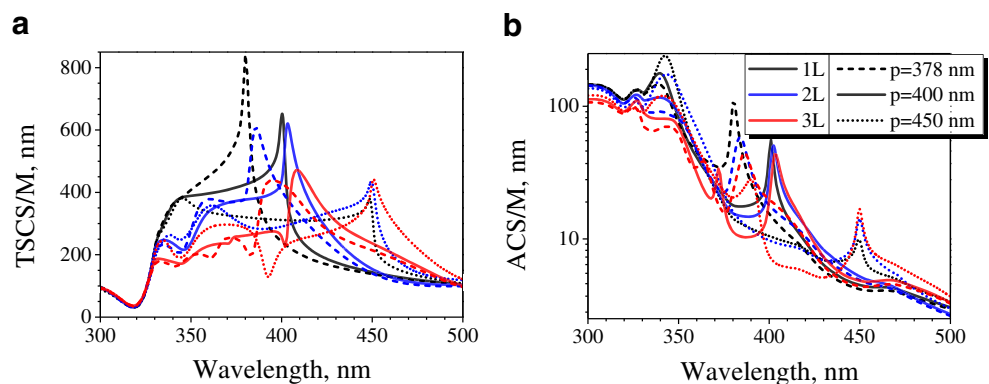
However, there is one other resonance peak on each plot, slightly red-shifted from the value of the main period, p_x ; this is the grating or lattice resonance. Note that the plasmon resonance has the shape close to Lorentzian while the grating resonance may display any of various Fano shapes, especially for the two-layer and three-layer gratings. The most intensive scattering occurs if the grating resonance is detuned from the plasmon resonance by some 20–30 nm to the red side. It is also worth to emphasize that the absorption is a finer instrument for locating the resonance wavelengths because it displays only the Lorentz-shape peaks.

Note also that the stacking of the gratings damps the plasmon-resonance peak in the per-wire TSCS and ACS at $\lambda = 340$ nm, apparently because of the shadowing of the deeper rows of nanowires by the frontal row.

In Fig. 4, we present the near-zone magnetic field amplitude patterns for two-layer (a) and three-layer (b) gratings with $p_x = 400$ nm and $p_y = 300$ nm at the wavelengths of the corresponding grating resonances, i.e., $\lambda = 403$ nm (a) and $\lambda = 409$ nm (b). One can see that the largest field maxima (bright spots) are located near the wires of the second from the illuminated side layer both for two-layer and three-layer gratings.

The field pattern has the features characteristic for the grating resonance of the first order, with other maxima between the wires that corresponds to the standing wave built on two oppositely propagating Floquet harmonics of the grating (see [17] for details).

Fig. 3 Normalized TSCS (a) and ACS (b) as a function of the wavelength for the single-layer, two-layer, and three-layer gratings of silver nanowires with radius 60 nm and periods $p_x = 378, 400,$ and 450 nm. Other parameters are $p_y = 5a,$ $M_{\text{layer}} = 100$. An H-polarized plane wave comes from the broadside direction



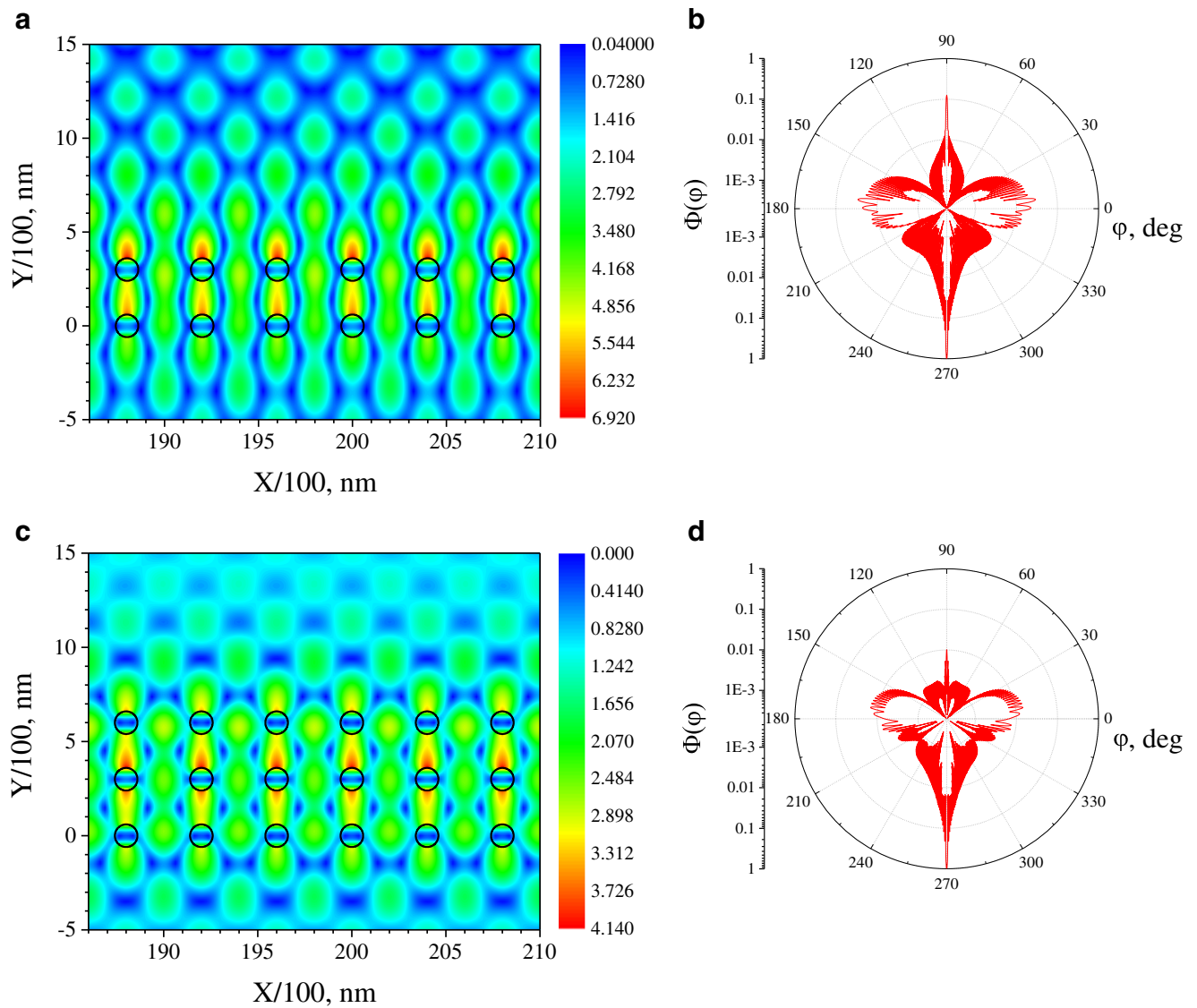


Fig. 4 Near-field patterns for five central periods (**a**, **c**) and far-field scattering patterns (**b**, **d**) for two-layer and three-layer gratings ($M_{layer}=100$) made of wires with $a=60$ nm and $p_x=400$ nm, $p_y=5a$ at the grating-resonance wavelengths 403 nm (**a**, **b**) and 409 nm (**c**, **d**)

Discrete Corners

Figures 5, 6, 7, and 8 show the results computed for several discrete right angle corners made of parallel silver wires with

$a=30$ and 60 nm and illuminated by the H-polarized plane wave.

In Fig. 5, presented are the plots of per-wire TSCS (a) and ACS (b) as a function of the wavelength for discrete corners of

Fig. 5 Normalized TSCS (**a**) and ACS (**b**) versus the wavelength for the right-angle discrete corners of 101 silver nanowires with $a=60$ nm and $p=400$ nm, for four angles of incidence

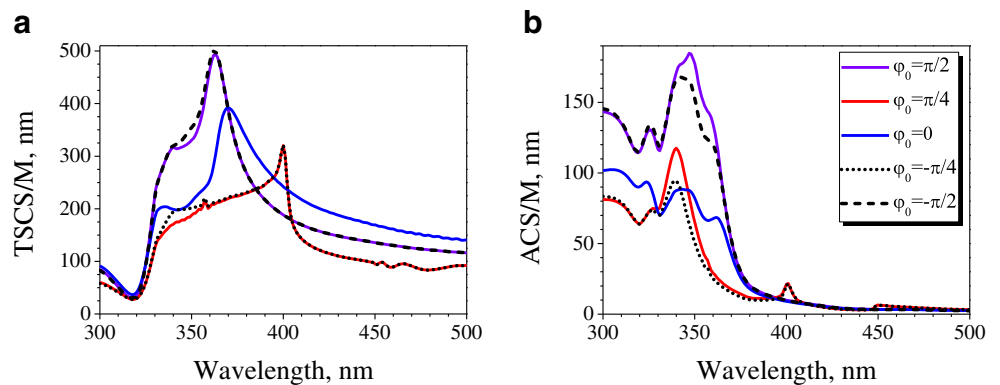


Fig. 6 Normalized TSCS (a, c) and ACS (b, d) as functions of wavelength for the right-angle discrete corners made of silver nanowires with radius 30 (a, b) and 60 nm (c, d). The plane H-polarized wave is incident along the line of symmetry of the corner

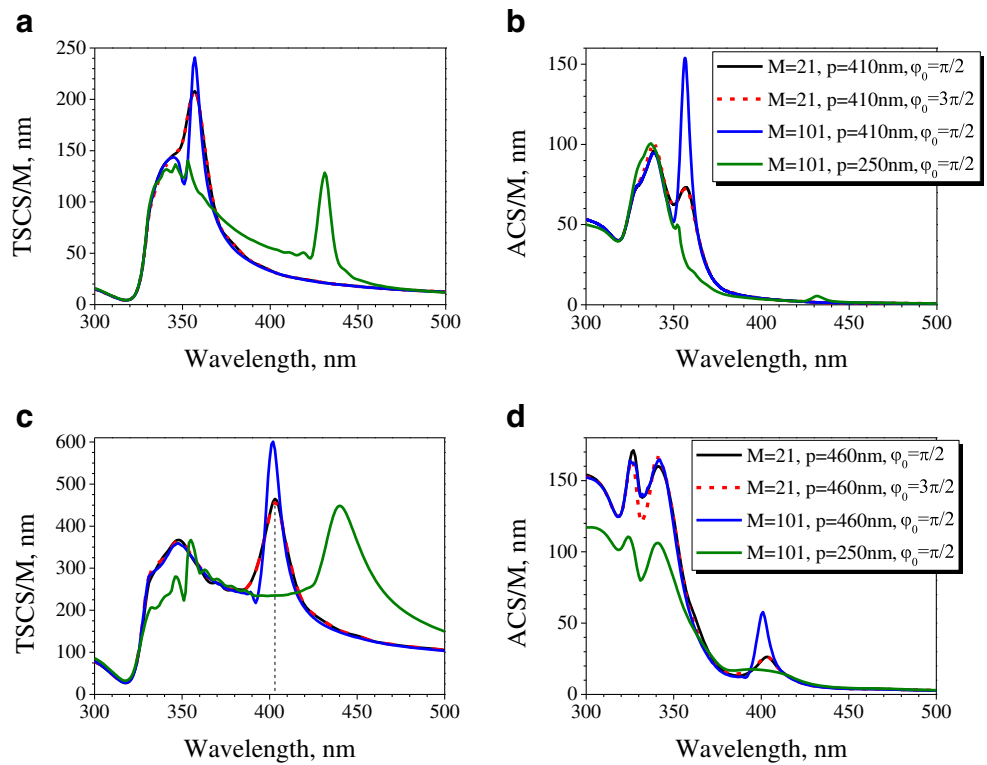
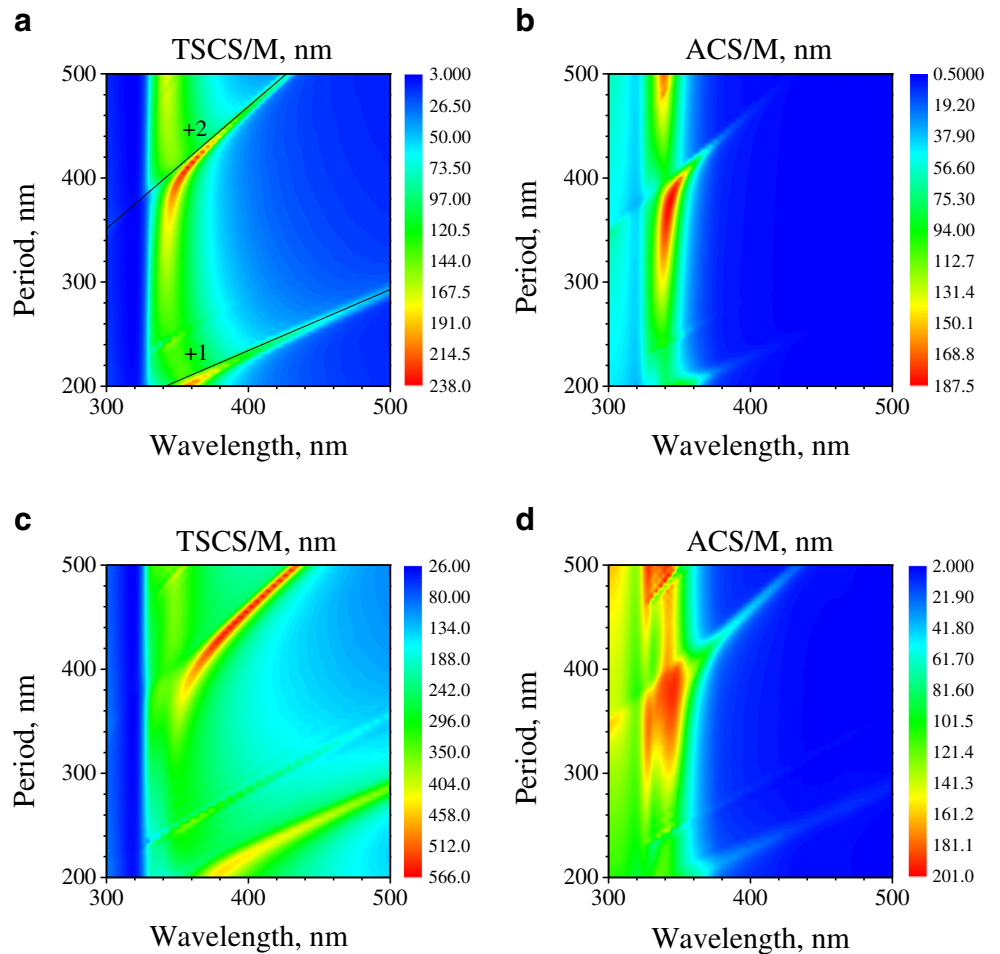


Fig. 7 Normalized TSCS (a, c) and ACS (b, d) as functions of period and wavelength for the right-angle discrete corners from 51 silver nanowires with radius 30 (a, b) and 60 nm (c, d)



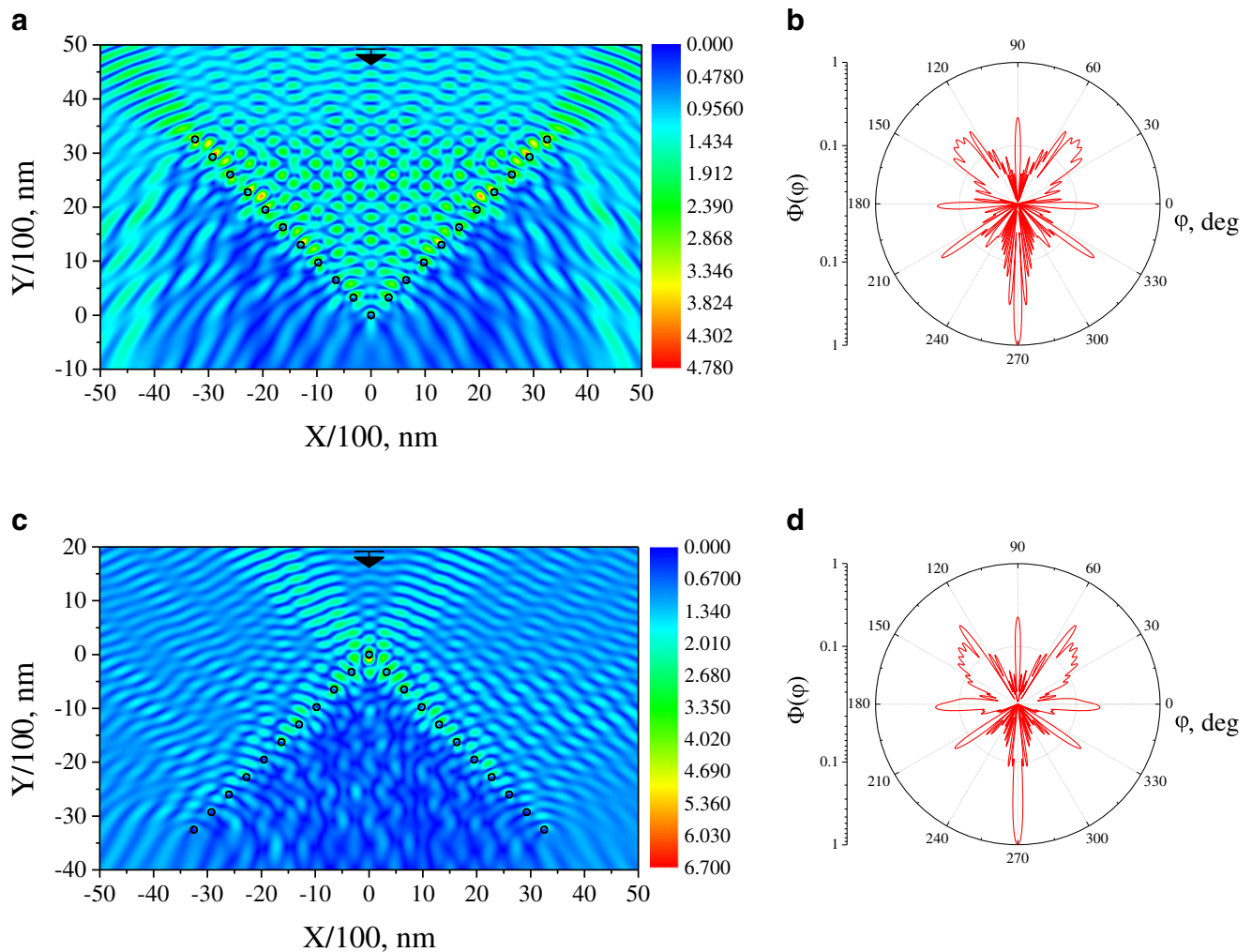


Fig. 8 Near fields (**a**, **c**) and far-field scattering patterns (**b**, **d**) for the discrete right corners made of 21 wires with $a=60$ nm and $p=460$ nm at the grating-resonance wavelength 403 nm, under symmetric incidence of the H-polarized plane wave, $\varphi_0=\pi/2$ (**a**) and $\varphi_0=-\pi/2$ (**b**)

101 silver wires with period 400 nm for different angles of incidence. Here, $\varphi_0=\pm\pi/2$ corresponds to the case of the incident wave “looking inside the corner” (this is default case) or “looking at the apex” in symmetric matter, respectively, and $\varphi_0=\pi/4$ corresponds to the wave incident along one of the corner arms. As in the previous sections, one can see two types of resonances on the TSCS plots in all cases.

The first broad resonance is at the wavelength near to 348 nm; this is the plasmon resonance which can be observed at the same location for a stand-alone silver wire. The second sharper resonance can be seen at 403 nm for $\varphi_0=\pi/4$, i.e., at the wavelength just above the period value because this is the normal incidence at one of corner’s arms. If φ_0 is arbitrary, then the wavelength of the grating resonance is shifted further from the period value. For instance, if $\varphi_0=0$ or $\pm\pi/2$, then it is located slightly above the value that corresponds to the expression for the +2nd Rayleigh anomaly (for a similar infinite grating) and the incidence angle of 45° : $\lambda_{RA}^{+2}=(p/2)[1+\cos(\pi/4)]$.

These two types of resonances are also well visible on the plots of ACS per one wire (Fig. 5b); here, the peaks at longer wavelengths are hindered by the lower values of the bulk absorption in silver. Note that the peak values of TSCS and ACS in the plasmon resonance at $\varphi_0=\pm\pi/2$ are approximately twice larger than at $\varphi_0=0$ or $\pm\pi/4$ because the former angle of incidence provides direct illumination of all wires while the latter only one arm of the corner.

In Fig. 6, similar dependences are presented for the two discrete corners made of 21 and 101 wires and illuminated by the plane wave in symmetric manner, coming either into the corner or on the apex. The plasmon resonance sits on its usual place while grating resonances of the +1 and +2 order are found at 440 and 357 or 403 nm, respectively; their locations are determined, in the leading term, by the equations for the +1st and +2nd Rayleigh anomalies with the incidence angle of 45° and the value of the period (250, 410, and 460 nm). The height and sharpness of these peaks become greater with

larger M . Note that the solid and dotted curves in Figs. 5 and 6 corresponding to two opposite directions of the incident wave propagation do not coincide. The difference is caused by non-zero absorption in the silver (for lossless scatterers similar two curves of TSCS coincide because of the reciprocity).

To visualize this enhancement in terms of two parameters, the wavelength and the period, Fig. 7a, c present reliefs of TSCS as a function of two arguments for discrete right-angle corners made of 51 silver wires of two values of radius, 30 and 60 nm, respectively.

Reliefs in Fig. 7b, d present similar information about ACS. We recall that here the incident plane wave “looks inside the corner” in symmetric manner with respect to its arms ($\varphi_0 = \pi/2$). On these reliefs, one can see two areas of intensive scattering. They stretch along the straight lines associated with the +2nd and +1st Rayleigh anomalies, where the corresponding Floquet harmonics are grazing.

In Fig. 8, presented are total-field near-zone and scattered-field far-zone patterns for discrete corners of 21 silver wires computed at the wavelength corresponding to the grating-resonance peak in TSCS shown in Fig. 6. One can see bright spots near the wires on the illuminated side of the corner arms and characteristic standing waves along the arms, formed by the grazing +2nd Floquet harmonics. More complicated four-wave standing pattern is seen inside the corner, formed by the specular reflections (i.e., by the bouncing 0th

Floquet harmonic). The configuration presented in Fig. 8b has the incident wave coming at the corner apex along the symmetry line (in Fig. 3c, this is the case of $\varphi_0 = -\pi/2$). In this case, in the grating resonance, there is a deep shadow inside the discrete corner of silver nanowires.

Note also intensive beams leaving the upper ends of the corner arms in the directions of $\varphi = \pi/4$ and $\varphi = 3\pi/4$. They appear due to the +2nd Floquet harmonics of the arm gratings in the grazing regime, and the corresponding sidelobes in the far-field scattering patterns $\Phi(\varphi)$ are the signature of the grating resonance.

Discrete Crosses

As another configuration where the grating resonances are well developed, we have studied the cross-shaped scatterers with M up to 101 wires in four arms of the cross, i.e., with one central wire and four 25-wire arms. As known, even several dozens of nanowires assembled in a straight chain are able to demonstrate visible peaks on these resonances in the scattering and absorption [17, 18]. The corresponding Q-factors grow up with larger M and approach their (finite) limit values associated with infinite gratings.

In Fig. 9, we present the spectra of per-wire TSCS (a, c) and ACS (b, d) for the sparse discrete crosses with the radius of each wire 30 nm (a-b) and 60 nm (c-d), in the visible

Fig. 9 Normalized TSCS (a, c) and ACS (b, d) as a function of the wavelength for several discrete crosses made of silver nanowires with radius 30 (a, b) and 60 nm (c, d)

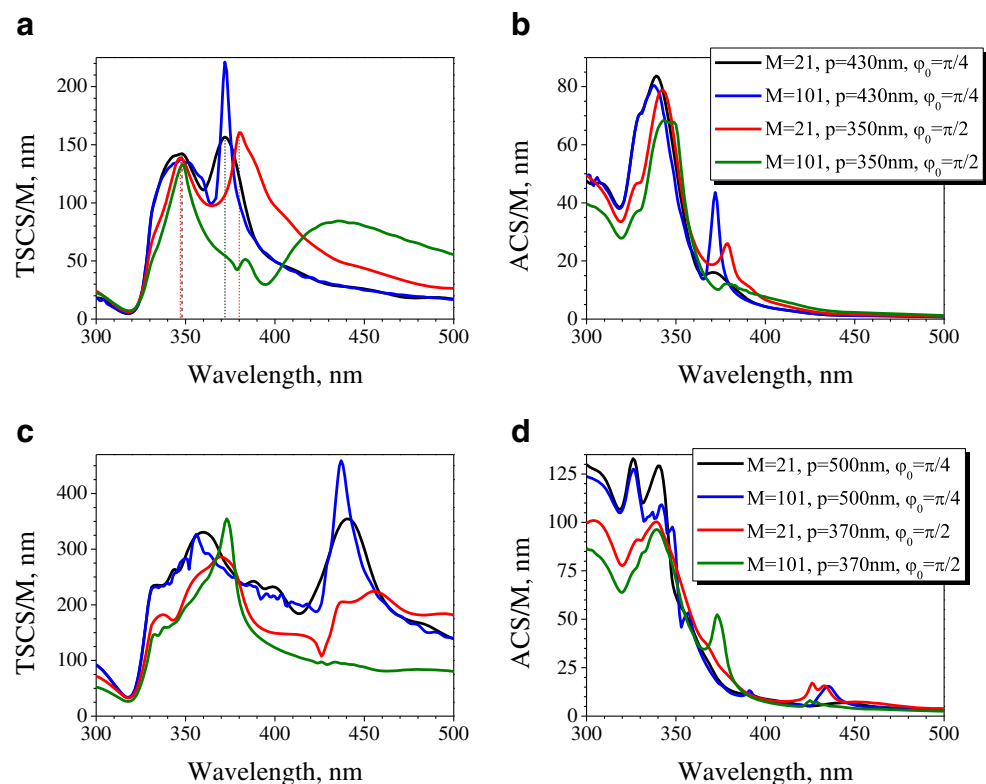


Fig. 10 Normalized TSCS (a, c) and ACS (b, d) as a function of the wavelength and the period for crosses made of 101 silver nanowires with radius 30 (a, b) and 60 nm (c, d), $\varphi_0 = \pi/2$

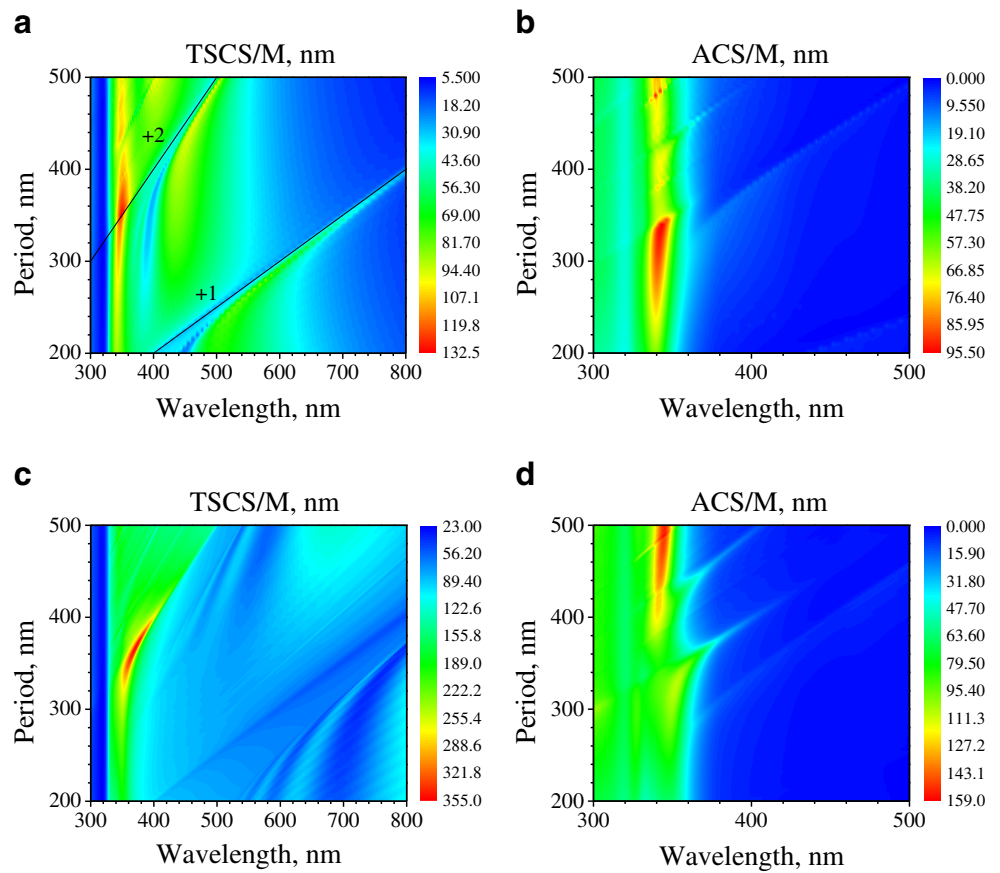
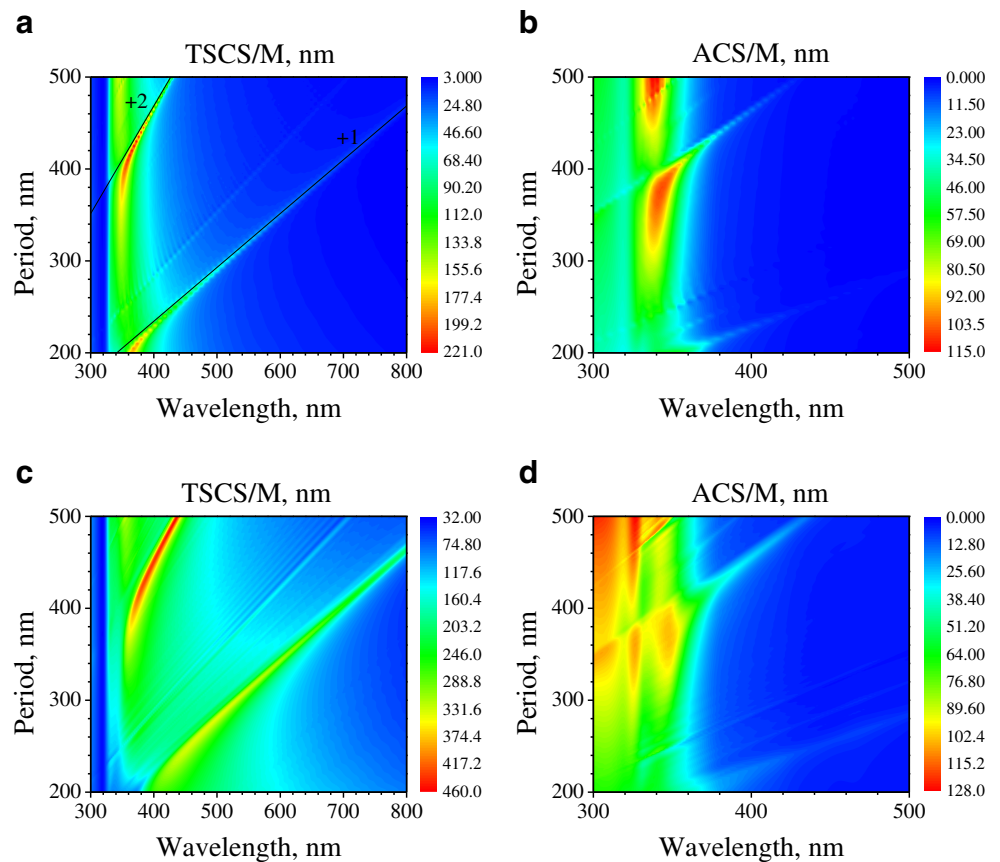


Fig. 11 The same as in Fig. 10 for “along-the-diagonal” incidence of plane wave, $\varphi_0 = \pi/4$



range, under two cases of the H-polarized plane wave incidence: along a cross arm ($\varphi_0 = \pi/2$) and along a diagonal ($\varphi_0 = \pi/4$). Note that the wavelength scan of ACS is a better tool for visualization of the resonances of all types than TSCS [6].

If a plane wave is incident along one of the cross arms, it means that the other two arms are illuminated in the broadside manner. From Fig. 9, one can also see that increasing the number of wires in the cross arm slightly inhibits the averaged value of TSCS and, especially, ACS in the plasmon resonance. Under such illumination, the principal grating-type resonance has the wavelengths near the period value, which has been taken, in computations, as $p = 350$ and 370 nm for crosses with wire radius 30 and 60 nm, respectively, i.e., just to the right from the plasmon resonance. Unlike plasmon, this resonance is getting sharper and more intensive if the number M increases.

If the plane wave illuminates the same discrete cross of silver wires along its diagonal, the mentioned-above resonances in the scattering and absorption are kept. The plasmon and the grating-type resonances are clearly identified by their different dynamics with respect to the growth of the number of wires. Here, the grating resonance is best visible near to the Rayleigh anomaly wavelength corresponding to the grazing regime of the +2nd Floquet harmonic.

The mentioned features of the light scattering and absorption by a discrete cross of silver wires are presented in more complete way in the reliefs in Figs. 10 and 11.

Here, they have been computed for the “along-the-arm” incidence and “along-the-diagonal” incidence, respectively, and two values of the wire radius, 30 and 60 nm. In each case, the bright “ridges” of enhanced scattering and absorption approach the straight lines corresponding to the Rayleigh anomalies if the period gets larger. The marks on reliefs

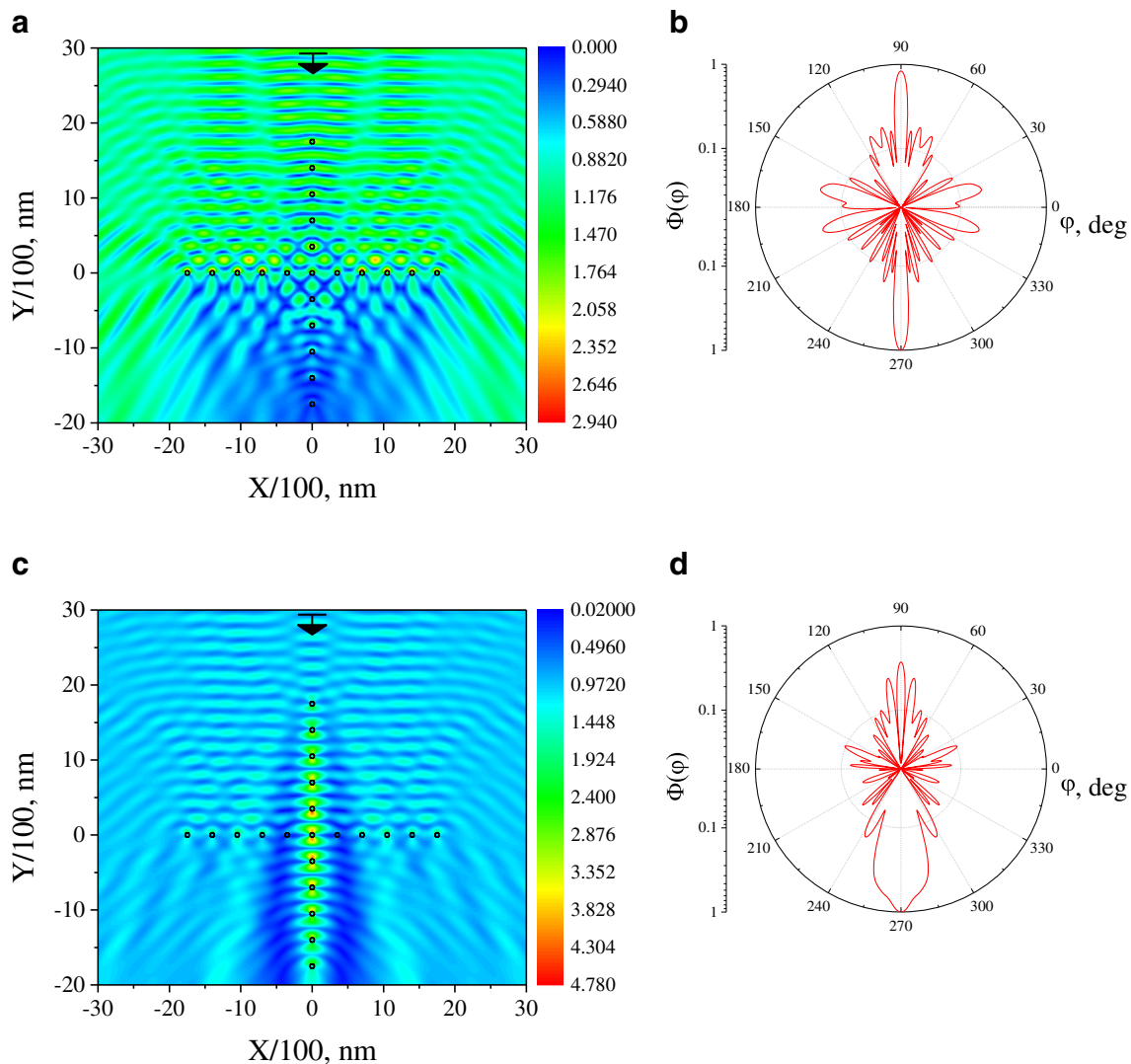


Fig. 12 Near-zone magnetic field amplitude patterns (a, c) and far-field scattering patterns (b, d) for the discrete crosses made of 21 wires with radius 30 nm and period 350 nm at the resonance wavelengths of 347 (a, b) and 380 nm (c, d)

indicate the indices of the Rayleigh anomalies, i.e., the numbers of Floquet harmonics which are grazing.

In Figs. 12 and 13, presented are the near-field amplitude patterns for several discrete crosses made of 21 silver wires with radius 30 nm at the wavelengths of plasmon resonances (Figs. 12a and 13a) and grating resonances (Figs. 12c and 13c) for two angles of the plane-wave incidence marked with black arrows.

In the plasmon resonances (see panels 12a and 13a), the near-field maxima are seen just at the illuminated side of each wire, and in the far zone, the specularly scattered wave is dominating. In contrast, in the grating resonance (see panels 12c and 13c), the illuminated arms of the cross demonstrate the Floquet-mode standing waves and inspection of the far-zone scattering pattern reveals characteristic strong sidelobes along the illuminated arms.

reached not in the plasmon resonance but in the grating resonance. This suggests using this type of resonance, instead of the conventional localized surface-plasmon one, in the advanced designs of surface-enhanced Raman scattering sensors and optical nanoantennas where enhancement of the near field is the primary goal.

Besides, a refractive-index sensor based on the grating resonance is also attractive [23, 43] because its bulk sensitivity is comparable with the conventional localized plasmon resonance-based sensors; however, the Q-factor can be much larger if the number of periods $M \gg 10$.

This combination boosts the figure-of-merit of such a sensor well over all other designs provided that the analyte medium makes a thick enough layer (in fact, thicker than the wavelength—see [23]). Note that if the sensing device uses a corner or cross-like configuration of nanograting, it is possible to place the light-collecting unit in the plane of one of the arms

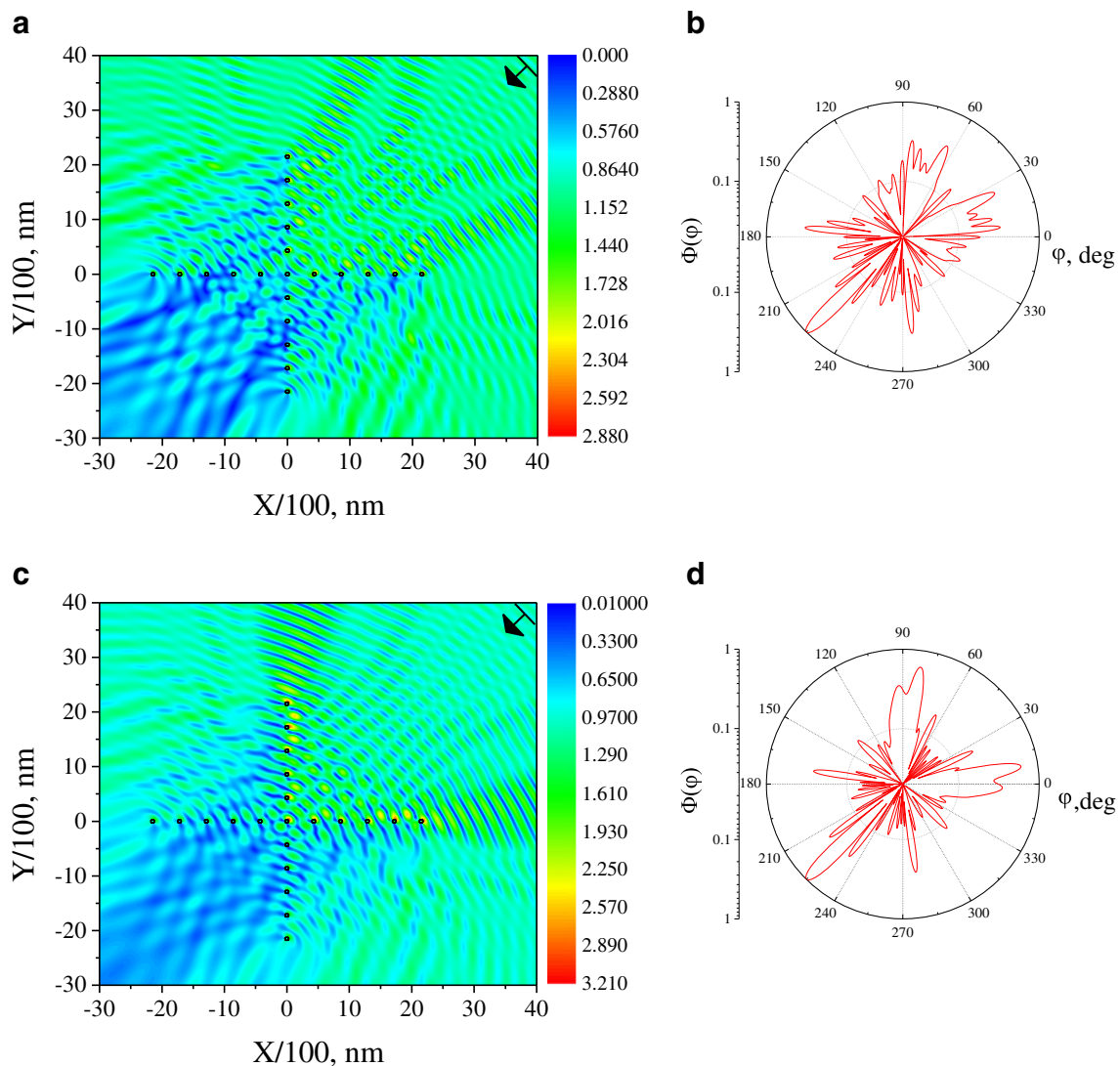


Fig. 13 Near-zone magnetic field amplitude and far-field patterns for the discrete crosses made of 21 wires with radius 30 nm and period 430 nm at the resonance wavelengths of 348 (a) and 372 nm (b)

Fig. 14 Normalized TSCS (a, c) and ACS (b, d) as functions of wavelength for the L2P gratings from $M=99$ nanowires with radius 30 (a, b) and 60 nm (c, d) with periods $p_1=420$ nm, $p_2=380$ nm under the different angles of H-wave incidence

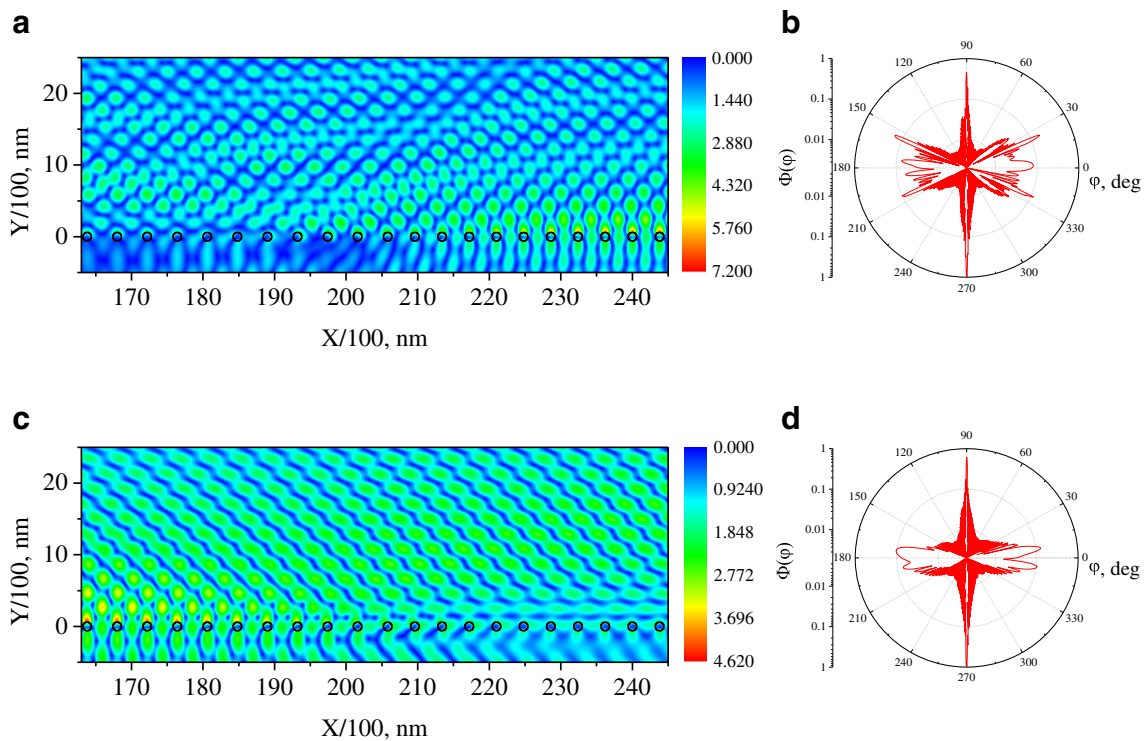
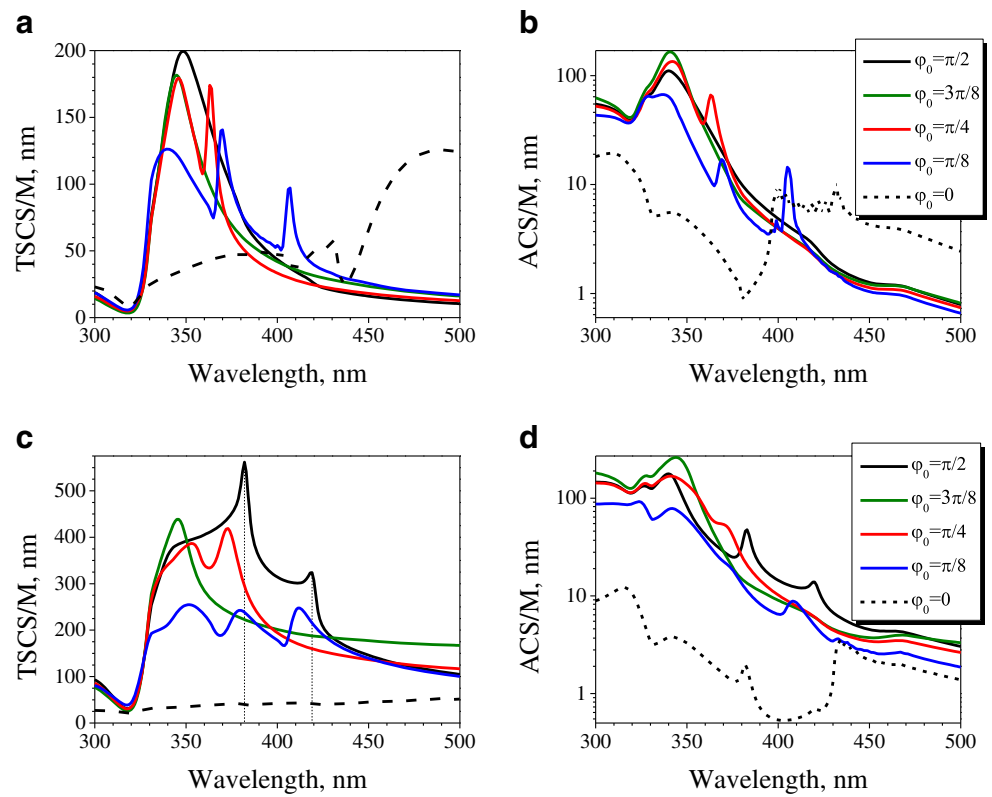


Fig. 15 Near-field amplitude and far-field patterns for the central wires of the L2P gratings from 99 wires with radius 60 nm and periods $p_1=420$ nm, $p_2=380$ nm at the grating-resonance wavelengths of 382 (a, b) and 419 nm (c, d) $\varphi_0=-\pi/2$

and, hence, spatially separate the directions of illumination and reception.

The grating resonances are also attractive in the design of nanoscale thin absorbers for novel solar cells. This is because they can be tuned, by adjusting the values of period, to specific wavelengths in order to provide higher absorption in the spectral bands where the surface-plasmon resonances are absent. Additional opportunities may appear if using more complicated configurations containing not one but several different period sub-gratings.

Double-Period Gratings: Inline and Stacked

We have also investigated two types of finite gratings composed of silver nanowires with two different periods: inline (we will label them as L2P) and stacked (this will be indicated as S2P).

In Fig. 14, the wavelength scans of the per-wire TSCS and ACS are presented, computed for the in-line grating with the left arm of $M=99$ wires having the period of 420 nm and the right arm of the equal number of wires having the period of 380 nm, for several angles of incidence from $\pi/2$ (normal or broadside incidence) to 0 (grazing or edge-on incidence).

In the broadside illumination case ($\varphi_0=\pi/2$), for the grating made of thin wires (30-nm radius, upper panels), one can see only one broad resonance at the usual plasmon wavelength. Thus, a grating of 50 thin silver wires is apparently too short to produce clear grating resonances.

However, if the angle of incidence gets smaller, then one and further two (at $\varphi_0=\pi/8$) additional sharp and intensive resonance peaks appear. They are the grating resonances at the wavelengths slightly to the red from the Rayleigh anomalies associated with +2nd and +1st Floquet harmonics at grazing.

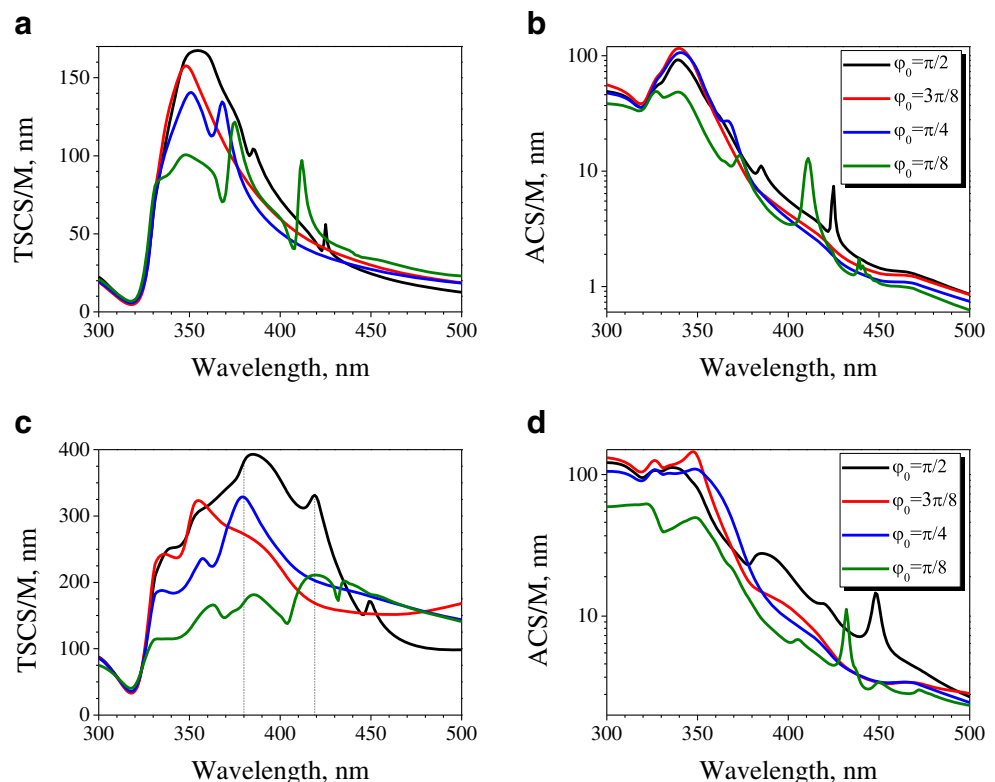
If the wires are twice thicker, of the 60-nm radius (lower panels), then even 50 wires is enough to produce well-visible grating resonances both at the normal and inclined incidence.

Note that for the in-line configuration of the composite grating, all the wires are illuminated and there is no significant shadowing effect except in the grazing-incidence case of $\varphi_0=0$.

The near-field patterns shown in Fig. 15 have been computed at the wavelengths of two grating-type resonances corresponding to the periods of the left and the right parts of the grating. Therefore, in panel (a), one can see that the right half of the grating is shining, with a characteristic Floquet-mode standing wave along the grating plane, while the left half is off the resonance and thus remains dark. In similar manner, in panel (c), it is the left half of the grating that is tuned to the incident wavelength and shines brightly and the right half is dark. Note that in each case, the shadow is deeper behind the dark part of the grating.

It is also helpful to visualize the far-field scattering patterns $\Phi(\varphi)$ at the resonance wavelengths. Figure 15b, d correspond to the near fields presented in Fig. 15a, c, respectively, and show these patterns in the normalized form. They display intensive narrow beams of the shadow and specularly reflected waves (0-th Floquet harmonics). Here, we remind

Fig. 16 The same as in the previous figure, however, for S2P gratings made of $M=105$ ($M_1=50$) nanowires, $p_y=5a$



that the total size of the composite grating is 99λ that makes it a truly large scatterer. Besides of them, in both cases, there are intensive beams along the plane of the grating—they appear because of the radiation of the ± 1 st Floquet harmonics from the ends of the finite resonant grating. Still besides, in the panel (b), one can see additional intensive sidelobes at the angles of approximately 28° to the plane of the grating that are absent in panel (d). These sidelobes correspond to the ± 1 st Floquet harmonics scattered by the non-resonant part of the composite grating. They are absent in panel (d) because here the mentioned Floquet harmonics are below cutoff as the wavelength is larger than the period of the non-resonant (dark) part of the grating.

Unlike in-line grating, for the stacked configuration of a composite two-period grating, the shadowing of a part of wires by the other directly illuminated part has certain effect. Here, in fact, only approximately a half of all wires are illuminated directly. This leads to the reduced (by some 20 %) off-resonance and in-resonance values of both TSCS and ACS per one wire with respect to the same values for a single silver wire—see Fig. 16. Still, one can see additional grating resonances appearing at the inclined incidence (for

thinner wires) or even at the normal incidence (for thicker wires) near to the wavelengths corresponding to the +2nd and +1st Floquet harmonics “passing over horizon.”

Note that if the wire radius is as small as 30 nm (upper panels), then the plasmon resonance remains a dominating feature in the spectral dependences of the per-wire scattering and absorption. This is apparently because 50 or 55 thin wires in a grating are still small number to produce more intensive grating resonances. Making them twice thicker, of 60-nm radius (lower panels) leads to the scattering spectrum where all resonances have comparable peak values; in the absorption spectrum, the plasmon resonance is still the most intensive one because the bulk losses in silver get larger in the violet range where it is located.

The near-field patterns shown in Fig. 17 have been computed again at the wavelengths of two grating-type resonances corresponding to the periods of the upper (illuminated) and the lower (shadowed) rows of the S2P grating. Therefore, in panel (a), one can see that the upper row of the grating is shining, while the lower row is shadowed and tuned off the resonance and thus remains dark. In contrast, in panel (c), it is the lower

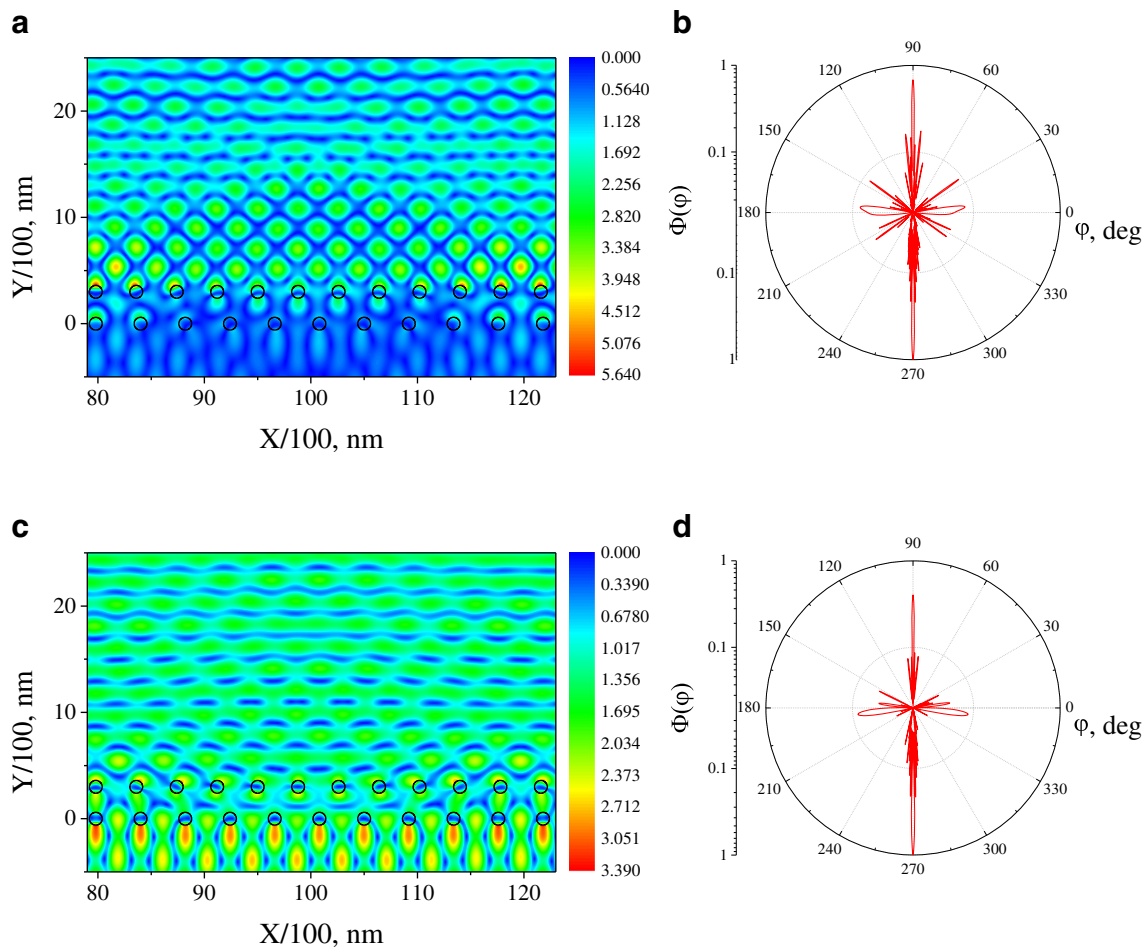


Fig. 17 Near-field amplitude and far-field patterns for the central wires of the S2P gratings from 105 wires ($M_1=50$) with radius 60 nm and periods $p_{x1}=420$ nm, $p_{x2}=380$ nm, $p_y=5a$ at resonant wavelengths 380 (a, b) and 419 nm (c, d), $\varphi_0=-\pi/2$

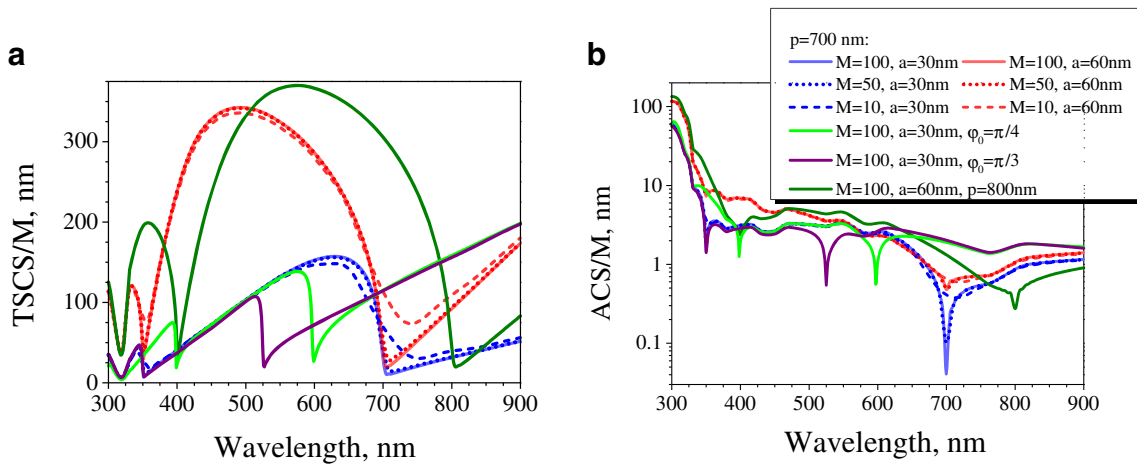


Fig. 18 Normalized TSCS (a) and ACS (b) as a function of the wavelength for the different linear gratings made of circular silver nanowires in the case of the normal incidence of an E-polarized plane wave

row of the grating that is tuned to the incident wavelength and therefore its shadowing by the upper row does not have any visible effect—the whole grating shines brightly.

The far-zone normalized scattering patterns at the same wavelengths are shown in panels (b) and (d). Their main

features are the narrow shadow and specular-reflection beams—they are the most intensive because of the $\sim 50\text{-}\lambda$ size of composite scatterer. The broader but also intensive beams are also present in the plane of the grating, produced by in-resonance Floquet harmonics.

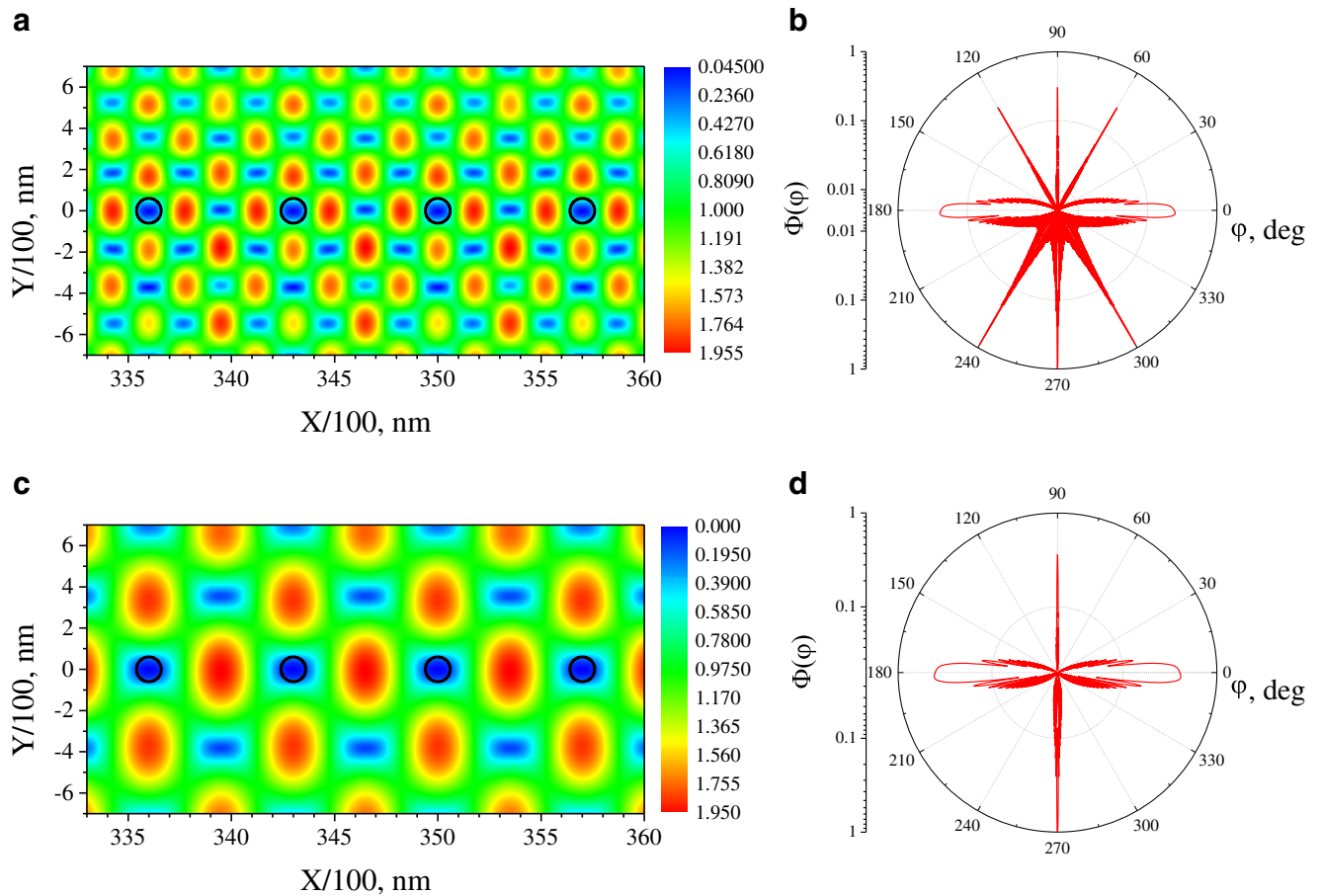


Fig. 19 Near and far-zone patterns for the central four wires of the grating of 100 wires with radius 60 nm and period 700 nm at the wavelengths of 350.1 (a, b) and 700.4 nm (c, d)

E-Polarization

For the sake of completeness, we have also investigated the scattering and absorption of the visible-range plane wave by simple one-period finite gratings of circular silver nanowires in the case of the E-polarization illumination (i.e., with the E-field along the wires). The wavelength dependences of the per-wire TSCS and ACS are presented in Fig. 18, where the broadside incidence is assumed ($\varphi_0 = \pi/2$). Here, the number of wires M varies from 10 to 100, and period is fixed at 800 nm. The wire radius values are given in the inset. Two curves corresponding to the inclined incidence are also added for comparison.

The plots in Fig. 18 quantify a well-known fact: in the case of the E-polarized illumination, even one metal wire is a strong non-resonant scatterer (no plasmon resonances). What is less predictable, any peaks associated with the grating resonances are also absent. The explanation follows from the fact established in [24]: the Q-factors of the grating resonances of E-type are lower, by a factor of $|\varepsilon|^2$, than the similar grating resonances of H-type. For the silver in the visible range, this factor can be as large as 400 at $\lambda = 800$ nm that spoil the resonances.

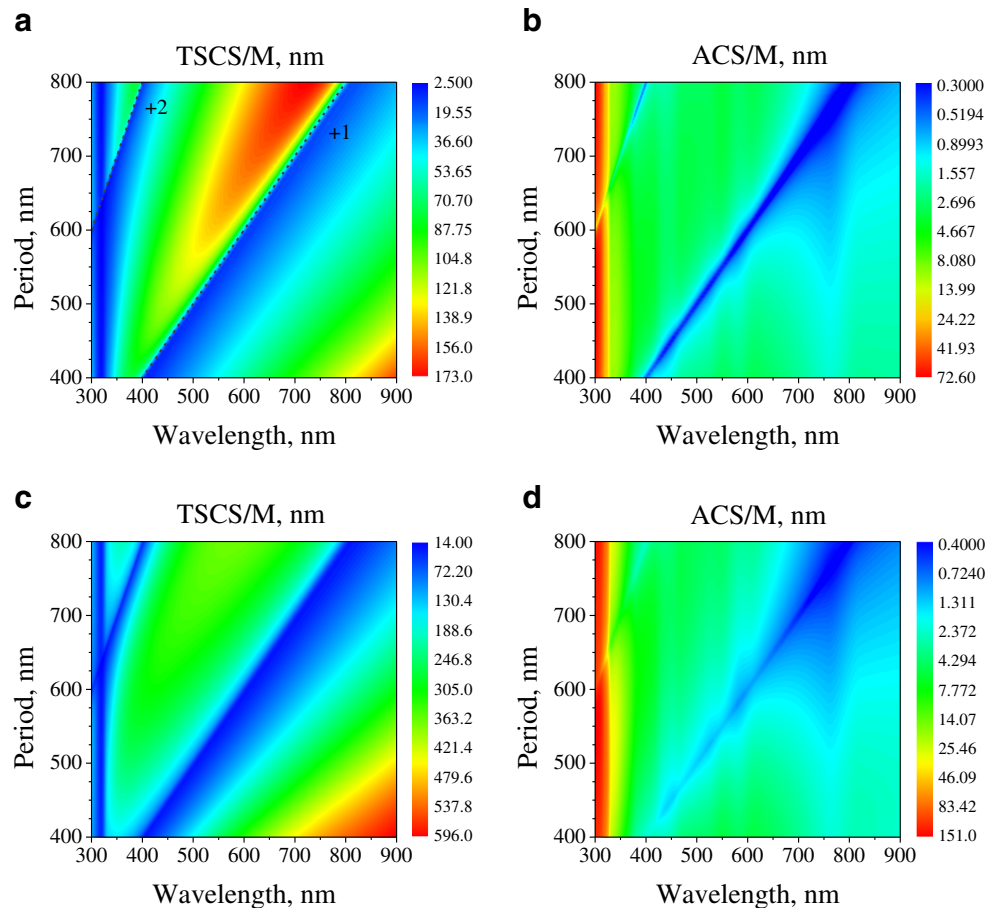
Thus, the only pronounced feature, in the E-case, of the spectral dependences of the per-wire scattering and absorption is sharp minima exactly at the wavelengths of Rayleigh anomalies. This is in agreement of the findings of the paper [42] where an infinite grating of rectangular gold bars was analyzed using a surface-impedance method.

This effect can be partially explained if the near field (in terms of the $|E_z|$) is visualized at the wavelengths corresponding to the scattering and absorption minima. Figure 19a, c correspond to the wavelength tuned to the ± 2 nd and ± 1 st Rayleigh anomalies, respectively.

As one can see, in each case, the lossy silver wires happen to be located in the deep minima of the electric field that entails reduced scattering and absorption.

In the far zone, the normalized scattering patterns shown in panels (b) and (d) demonstrate two intensive narrow beams, shadow and specular-reflection ones (corresponding to the 0-th Floquet harmonics) plus two broader sidelobes in the plane of the grating caused by the grazing Floquet harmonics. In panel (b), additionally, there are four narrow sidelobes corresponding to the ± 1 st Floquet harmonics in the scattered field; such lobes are absent in panel (d) because here they are below

Fig. 20 Reliefs of normalized TSCS (a, c) and ACS (b, d) for the linear gratings from 50 wires of radius 30 (a, b) and 60 nm (c, d), in the case of E-polarization



grazing. Note that the amplitudes of all beams are much smaller than in the grating resonances on the same gratings in the H-polarization regime (see above).

More information on this effect can be inferred from the reliefs of the per-wire TSCS and ACS as a function of two variables: wavelength and period (Fig. 20). The upper and lower panels correspond to the gratings of 30- and 60-nm wires, respectively. As visible, at the Rayleigh-anomalies wavelengths, both the scattering and the absorption are significantly damped.

Conclusions

Today, periodic arrays of noble-metal nanogratings are used mainly in two application areas: the nanosensors of the changes in refractive index of host medium and the ultra-thin absorbers for novel solar cells. In the first case, the principle of operation is based on measuring the position of the plasmon peak in the scattering or extinction. This is considered as key enabling technology in biological and chemical nanosensing [43–46]. The gratings of a few hundred metal particles were originally viewed as a way to collect the many plasmon-resonance contributions of the scattered light. The grating-mode resonances were, therefore, a sort of parasitic phenomenon. However, their higher Q-factors have attracted attention of researchers and recently new type of refractive-index sensors has been proposed [23, 43, 44]. Additionally, extraordinary near-field enhancement in the larger domain than for the surface plasmons makes the grating resonances attractive for advanced substrates for the surface-enhanced Raman scattering [2].

In the second case, novel solar-cell absorbers were at first using the surface-plasmon resonances on randomly distributed metal particles embedded into a dielectric layer [47]. However, their periodic placement has soon revealed the role of the grating resonances. Indeed, combining nanogratings with several values of periodicity, one can introduce additional absorption resonances and hence engineer the spectral behavior of the absorber [48, 49].

The optical properties of large periodic ensembles of coupled metal wires are quite different from those of dimers, short arrays, or small clusters of them. The latter configurations demonstrate only the low-Q resonances on the localized surface plasmon modes, which have been well documented. The chains, arrays, and gratings of many dozens and hundreds of such wires remain less studied and possess additionally the grating-mode resonances, which are caused by the periodicity and have much higher Q-factors. Although these resonances have been frequently mixed up with Rayleigh anomalies or interpreted as specific plasmons, today

their interpretation is less controversial. We have presented results of accurate calculations of the electromagnetic wave scattering and absorption by several different periodically structured configurations made of many silver nanowires, in the visible range: corners, crosses, and finite gratings with two different periods. We would like to emphasize that our numerical results have been computed using the algorithm whose convergence is guaranteed by mathematical theorems.

It has been demonstrated that corners and crosses of silver wires provide enhanced scattering and absorption in wider wavelength ranges and are less dependent on the direction of arrival of the incident illumination than a linear chain of nanowires. Further opportunities for efficient spectral engineering of enhanced scattering and absorption have been demonstrated on the finite wire gratings containing two different periodic sub-arrays, which support two separate types of grating resonances. These effects can find applications, for instance, in the design of more efficient multi-wavelength optical sensors and plasmonic solar cell absorbers.

Acknowledgment This work has been partially supported by the National Academy of Sciences of Ukraine via the Target Program “Nanotechnologies and Nanomaterials,” the European Science Foundation via the travel grants of the Networking Programme “Newfocus,” and the International Visegrad Fund and the Rennes-Metropole Association via the Mobility Grants to the first author.

References

- Ohtaka K, Numata H (1979) Multiple scattering effects in photon diffraction for an array of cylindrical dielectrics. *Phys Lett* 73-A(5–6):411–413
- Carron KT, Fluhr W, Meier M, Wokaun A, Lehmann HW (1986) Resonances of two-dimensional particle gratings in surface-enhanced Raman scattering. *J Opt Soc Am B* 3(3):430–440
- Zinenko TL, Nosich AI, Okuno Y (1998) Plane wave scattering and absorption by resistive-strip and dielectric-strip periodic gratings. *IEEE Trans Antennas Propag* 46(10):1498–1505. In the H-case, the grating resonances were missed because of too coarse computation grid, in frequency
- Christ A, Zentgraf T, Kuhl J, Tikhodeev SG, Gippius NA, Giessen H (2004) Optical properties of planar metallic photonic crystal structures: experiment and theory. *Phys Rev B* 70(12):125113/1–125113/15
- Zou S, Janel N, Schatz GC (2004) Silver nanoparticle array structures that produce remarkably narrow plasmon lineshapes. *J Chem Phys* 120:10871/5
- Felidj N, Laurent G, Aubard J, Levi G, Hohenau A, Krenn JR, Aussenegg FR (2005) Grating-induced plasmon mode in gold nanoparticle arrays. *J Chem Phys* 123:221103/1–221103/5
- Gomez-Medina R, Laroche M, Saenz JJ (2006) Extraordinary optical reflection from sub-wavelength cylinder arrays. *Opt Exp* 14(9):3730–3737
- Garcia de Abajo FJG (2007) Colloquium: light scattering by particle and hole arrays. *Rev Mod Phys* 79(4):1267–1289
- Marinica DC, Borisov AG, Shabanov SV (2007) Second harmonic

- generation from arrays of subwavelength cylinders. *Phys Rev B* 76(8):085311/10
10. Chu Y, Schonbrun E, Yang T, Crozier KB (2008) Experimental observation of narrow surface plasmon resonances in gold nanoparticle arrays. *Appl Phys Lett* 93(18):181108/3
 11. Kravets VG, Schedin F, Grigorenko AN (2008) Extremely narrow plasmon resonances based on diffraction coupling of localized plasmons in arrays of metallic nanoparticles. *Phys Rev Lett* 101:087403/4
 12. Auguie B, Barnes WL (2008) Collective resonances in gold nanoparticle arrays. *Phys Rev Lett* 101:143902/4
 13. Gadsdon MR, Hooper IR, Sambles JR (2008) Optical resonances on subwavelength lamellar gratings. *Opt Exp* 16(26):22003–22028
 14. Gao H, McMahon JM, Lee MH, Henzie J, Gray SK, Schatz GC, Odom TW (2009) Rayleigh anomaly—surface plasmon polariton resonances in palladium and gold subwavelength hole arrays. *Opt Exp* 17(4):2334–2340
 15. Giannini V, Vecchi G, Gomez Rivas J (2010) Lighting up multipolar surface plasmon polaritons by collective resonances in arrays of nanoantennas. *Phys Rev Lett* 105:266801/4
 16. Byelobrov VO, Ctyroky J, Benson TM, Sauleau R, Altintas A, Nosich AI (2010) Low threshold lasing eigenmodes of an infinite periodic chain of quantum wires. *Opt Lett* 35(21):3634–3636
 17. Natarov DM, Byelobrov VO, Sauleau R, Benson TM, Nosich AI (2011) Periodicity-induced effects in the scattering and absorption of light by infinite and finite gratings of circular silver nanowires. *Opt Exp* 19(22):22176–22190
 18. Natarov DM, Sauleau R, Nosich AI (2012) Periodicity-enhanced plasmon resonances in the scattering of light by sparse finite grids of circular silver nanowires. *IEEE Photonics Tech Lett* 24(1):43–45
 19. Byelobrov VO, Benson TM, Nosich AI (2012) Binary grating of subwavelength silver and quantum wires as a photonic-plasmonic lasing platform with nanoscale elements. *IEEE J Sel Top Quant Electron* 18(6):1839–1846
 20. Rodriguez SRK, Schaafsma MC, Berrier A, Rivas JG (2012) Collective resonances in plasmonic crystals: size matters. *Phys B* 407:4081–4085
 21. Teperik TV, Degiron A (2012) Design strategies to tailor the narrow plasmon-photonic resonances in arrays of metallic nanoparticles. *Phys Rev B* 86:245425/5
 22. Ghenuche P, Vincent G, Laroche M, Bardou N, Haidar R, Pelouard J-L, Collin S (2012) Optical extinction in a single layer of nanorods. *Phys Rev Lett* 109:143903/5
 23. Ricciardi A, Savoia S, Crescitelli AI, Esposito E, Galdi V, Cusano A (2013) Surface vs. bulk sensitivity of sensors based on Rayleigh anomalies in metallic nanogratings. *Proc SPIE Opt Sensors*. 8774: art. no. 87741 V/8.
 24. Zinenko TL, Marciniak M, Nosich AI (2013) Accurate analysis of light scattering and absorption by an infinite flat grating of thin silver nanostrips in free space using the method of analytical regularization. *IEEE J Sel Top Quant Electron* 19: (3), art. no. 9000108/8.
 25. Shapoval OV, Nosich AI (2013) Finite gratings of many thin silver nanostrips: optical resonances and role of periodicity. *AIP Adv* 3(4): 042120/13
 26. Cao Q, Lalanne P (2002) Negative role of surface plasmons in the transmission of metallic gratings with very narrow slits. *Phys Rev Lett* 88:057403/4
 27. Lord Rayleigh (1907) On the dynamical theory of gratings. *Proc Roy Soc Lond A*:79:399–416
 28. Martin OJF (2003) Plasmon resonances in nanowires with non-regular cross-section. In: Tominaga J, Tsai DP (Eds.) *Optical Nano-Technologies, Topics Appl. Phys.*, Springer, 88: 183–210.
 29. Fredkin DR, Mayergoyz I (2003) Resonant behavior of dielectric objects (electrostatic resonances). *Phys Rev Lett* 91: 3902–3905
 30. Kottman JP, Martin OJF (2001) Plasmon resonant coupling in metallic nanowires. *Opt Express* 8:655–663
 31. Stognii NP, Sakhnenko NK (2013) Plasmon resonances and their quality factors in a finite linear chain of coupled metal wires. *IEEE J Sel Top Quant Electron* 19:(3), art. 4602207/7.
 32. Biris CG, Panoi NC (2010) Nonlinear pulsed excitation of high-Q optical modes of plasmonic nanocavities. *Opt Express* 18(16): 17165–17179
 33. Twersky V (1952) On a multiple scattering theory of the finite grating and the Wood anomalies. *J Appl Phys* 23:1099–1118
 34. Ragheb HA, Hamid M (1985) Scattering by N parallel conducting circular cylinders. *Int J Electron* 59:407–421
 35. Felbacq D, Tayeb G, Maystre D (1994) Scattering by a random set of parallel cylinders. *J Opt Soc Am A* 11:2526–2538
 36. Elsherbeni AZ, Kishk AA (1992) Modeling of cylindrical objects by circular dielectric and conducting cylinders. *IEEE Trans Antennas Propag* 40:96–99
 37. Guida G, Maystre D, Tayeb G (1997) Enhanced normal scattering by lacunary gratings. *J Opt Soc Am A* 14(2):430–436
 38. She H-Y, Li L-W, Chua SJ, Ewe W-B, Martin OJF, Mosig JR (2008) Enhanced backscattering by multiple nanocylinders illuminated by TE plane wave. *J Appl Phys* 104:064310/7
 39. Antoine X, Geuzaine C, Ramdani K (2010) Computational methods for multiple scattering at high frequency with applications to periodic structure calculations. In: Ehrhardt M (Ed.) *Progress in Computational Physics (PiCP)*, Bentham Science Publ., pp. 73–107.
 40. Bohren CF, Huffman DR (2007) *Absorption and Scattering of Light by Small Particles*. Wiley, NY
 41. Johnson PB, Christy RW (1972) Optical constants of the noble metals. *Phys Rev B* 6:4370–4378
 42. Lochbihler H (2009) Enhanced transmission of TE polarized light through wire gratings. *Phys Rev B* 79(24):245427/8, Here, the E-polarization case is considered
 43. Offermans P, Schaafsma MC, Rodriguez SRK, Zhang Y, Crego-Calama M, Brongersma SH, Gomez Rivas J (2011) Universal scaling of the figure of merit of plasmonic sensors. *ACS Nano* 5(6):5151–5157
 44. Limaj O, Lupi S, Mattioli F, Leoni R, Ortolani M (2011) Midinfrared surface plasmon sensor based on a substrateless metal mesh. *Appl Phys Lett* 98(9):091902/3
 45. Nikitin AG, Kabashin AV, Dallaporta H (2012) Plasmonic resonances in diffractive arrays of gold nanoantennas: near and far field effects. *Opt Express* 20(25):27941–27952
 46. Murai S, Verschuuren MA, Lozano G, Pirruccio G, Rodriguez SRK, Gomez Rivas J (2013) Hybrid plasmonic-photonic modes in diffractive arrays of nanoparticles coupled to light-emitting optical waveguides. *Opt Express* 21(4):4250–4262
 47. Mokkaapati S, Catchpole KR (2012) Nanophotonic light trapping in solar cells. *J Appl Phys* 112(10):101101/19
 48. Li XH, Sha WEI, Choy WCH, Fung DDS, Xie FX (2012) Efficient inverted polymer solar cells with directly patterned active layer and silver back grating. *ACS J Phys Chem* 116(12): 7200–7206
 49. Massiot I, Colin C, Sauvan C, Lalanne P, Roca i Cabarrocas P, Pelouard J-L, Collin S (2013) Multi-resonant absorption in ultrathin silicon solar cells with metallic nanowires. *Optics Express* 21(S3):A372-A381